Renewable Energy 232 (2024) 121061

Contents lists available at ScienceDirect

Renewable Energy

journal homepage: www.elsevier.com/locate/renene

Simulation and experimental study of thermoelectric generators with an axial gradient metal foam heat exchanger

Wenlong Yang [a,b], Changjun Xie [a,b], Chenchen Jin [b], Wenchao Zhu [c,*], Yang Li [d], Xinfeng Tang [c,**]

[a] Hubei Key Laboratory of Advanced Technology for Automotive Components, Wuhan University of Technology, Wuhan, 430070, China
[b] School of Automation, Wuhan University of Technology, Wuhan, 430070, China
[c] State Key Laboratory of Advanced Technology for Materials Synthesis and Processing, Wuhan University of Technology, Wuhan, Hubei, 430070, China
[d] Department of Electrical Engineering, Chalmers University of Technology, Gothenburg, 41258, Sweden

ARTICLE INFO

Keywords:
Thermoelectric generator
Core heat transfer enhancement
Metal foam
Gradient structure
Waste heat recovery

ABSTRACT

The utilization of metal foam for heat transfer augmentation is regarded as a highly efficient technique, albeit associated with significant pressure losses. To enhance the feasibility of employing metal foam in thermoelectric generators and mitigate the high-pressure drop, we propose an enhancement strategy involving the partial axial filling of gradient metal foam. Both analytical modeling and experimental investigation were employed to evaluate the effects of porosity, pore density, and gradient structure at various filling rates on the overall performance of thermoelectric generators. The results show that arranging metal foam with increasingly high frame density in the direction of fluid flow, rather than adopting increasingly sparse or constant structures, leads to improved voltage uniformity and reduced pressure drop. A positive gradient configuration with a pore density distribution of 5-10-20 PPI yielded the highest net power at 118.3 W, which is 12.5 % higher than that of metal foam with constant 20 PPI. Ultimately, empirical verification substantiates the comprehensive performance advantages of positive gradient configuration. For filling rates of 30 %, 60 %, and 100 %, pressure drop is reduced by 35.9 %, 33.4 %, and 29.2 %, respectively, in comparison to constant 20 PPI metal foam, despite a modest reduction in output power, which remains less than 3 %.

Nomenclature

a_{sv}	area per unit volume ($m^2\ m^{-3}$)	δ	thickness (m)
c_p	specific heat capacity (kJ kg^{-1} K^{-1})	ε	density (kg m^{-3})
d	*pn* leg dimension (m)	λ	thermal conductivity (W m^{-1} K^{-1})
D_{hy}	hydraulic diameter (m)	μ	dynamic viscosity (Pa s)
f	friction coefficient	ρ	electrical resistivity (Ω m)
g	inertia coefficien	Φ	interstitial heat transfer coefficient (W m^{-2} K^{-1})
h	convective heat transfer coefficient (W m^{-2} K^{-1})	ω	porosity
H	height (m)	Ω	foam-finned surface efficiency
I	current (A)	ϕ	permeability (m^2)
k	equivalent heat transfer coefficient (W m^{-2} K^{-1})	*Subscript*	
K	thermal conductance (W K^{-1})	c	cold side
l	equivalent fin length (m)	ce	ceramic
		ct	contact resistance

(*continued on next column*)

(*continued*)

L	length (m)	$conv$	convective resistance
m	mass flow rate (kg s^{-1})	cu	copper
N	grid number	f	hot fluid
Nu	Nussel number	h	hot side
ΔP	pressure drop (Pa)	hex	heat exchanger
P	power (W)	L	load resistance
Pr	Prandtl number	mf	metal foam
q	heat flow (W)	n	*n*-type semiconductor leg
R	electrical resistance (Ω)	p	*p*-type semiconductor leg
Re	Reynolds number	pn	a *pn* couple value
Rt	thermal resistance (m^2 K W^{-1})	sub	substrate layer
S	heat transfer area (m^2)	w	water-cooled heat sink
t	fiber thickness (m)	x	x-direction
T	temperature (K)	y	y-direction
ΔT	temperature difference (K)	*Abbreviations*	
v	flow velocity (m s^{-1})	GMF	graded metal foam

(*continued on next page*)

* Corresponding author. Wuhan university of technology, No.122, Luoshi road, Hongshan district, Wuhan city, Hubei province, China.
** Corresponding author. Wuhan university of technology, No.122, Luoshi road, Hongshan district, Wuhan city, Hubei province, China.
E-mail addresses: wenlongyang@whut.edu.cn (W. Yang), jackxie@whut.edu.cn (C. Xie), 1528923556@qq.com (C. Jin), zhuwenchao@whut.edu.cn (W. Zhu), yangli@ieee.org (Y. Li), tangxf@whut.edu.cn (X. Tang).

https://doi.org/10.1016/j.renene.2024.121061
Received 18 March 2024; Received in revised form 12 June 2024; Accepted 22 July 2024
Available online 23 July 2024

(*continued*)

W	width (m)	HTC	heat transfer coefficient
Greek symbols		PPI	number of pores per inch
α	Seebeck coefficient (V K^{-1})	TEG	thermoelectric generator
γ	voltage uniformity coefficient	TEM	thermoelectric module

1. Introduction

Over the past several decades, the advancement of industrial and transportation systems, as well as the amelioration of human existence, have predominantly relied on the extensive utilization of fossil fuels. However, in order to achieve the net-zero carbon emissions target by 2050, the share of electricity in the total energy consumption should be increased to nearly half. This electricity must be derived from clean sources rather than fossil fuels [1]. As global regulations on carbon emissions are becoming increasingly stringent, the exploration of innovative energy supply methods based on renewable sources holds promise [2].

To address the incessant growth in energy demand, an alternative approach involves reducing additional energy requirements by enhancing the energy efficiency of the energy system. Thermoelectric Generators (TEGs) are widely employed for this purpose due to their advantageous characteristics, including long operational lifespans, high environmental safety, strong adaptability, and the absence of chemical reactions [3]. According to temperature ranges, waste heat can be categorized into low-temperature (<500 K), medium-temperature (500–923 K), and high-temperature (>923 K) waste heat. TEGs play a pivotal role in low-temperature waste heat recovery systems, as they operate based on the Seebeck effect, generating power with a temperature differential formed at their two ends. Therefore, TEGs find application in various domains, such as solar thermal energy [4], exhaust heat recovery [5], industrial waste heat [6], wearable electronic devices [7], wireless sensor power systems [8], and even natural gas cold energy recovery [9].

1.1. Literature review

In recent years, substantial efforts have been directed towards optimizing TEGs across various domains to attain superior output performance, and yet there remains significant room for improvement. Generally, within the realm of thermoelectrics, one can delineate three mutually influential domains of research: materials science, device-level design, and system-level design [10].

Within the domain of materials science, an effective avenue to enhance the conversion efficiency lies in the elevation of the optimal "figure of merit" (ZT) of materials. ZT is the outcome of the competition between electronic and thermal transport within the material [11]. Due to a myriad of innovative strategies, the ZT values of TE materials have witnessed a rapid ascent [12,13]. Particularly, the creation of nanostructured materials has made significant enhancements in TE performance achievable. Researchers have unveiled that, in the presence of particular transient heat sources, the average transient efficiency of thermoelectric (TE) components exceeds the steady-state efficiency. To enhance the dynamic performance of thermoelectric modules, a method involving periodic heating has been advanced [14]. This results in a 52.93 % increase in time-averaged ZT values and a 43.59 % boost in equivalent conversion efficiency.

Beyond ZT, device-level design in thermoelectrics also relies on other critical factors such as leg geometry dimensions [15,16], thermal boundary conditions [17], and thermal contact resistance [18], which dictate the device's performance. Several different variable cross-sectional thermoelectric legs have been introduced, which, while keeping the volume of thermoelectric materials constant, augment the temperature gradient in high-performance regions by reducing the cross-sectional area. Optimized operating temperature differentials and output power can be maximized by 73.14 % and 20.13 %, respectively [19]. Notably, for common commercial BiTe-based thermoelectric materials, it has been observed that, due to the low electrical resistance and high thermal conductivity of *n*-type thermoelectric materials, their efficiency and recovery power are superior. In our previous study, it was found that for BiTe-based annular asymmetric TEGs [20], the optimal size ratio of *n*-type and *p*-type thermoelectric elements is less than 1.

To maximize the performance of TEGs, it is imperative to concurrently consider material properties and operational conditions. This is because every TE material exhibits a peak ZT value within a specific temperature range. In applications with substantial temperature differentials, a suitable solution is to fabricate segmented thermoelectric elements employing different materials [21] or utilize thermoelectric modules arranged in a cascaded configuration [22] suitable for varying temperature ranges. However, the use of cascaded modules presents challenges to the entire system, including increased thermal contact resistance and thermal losses [10].

By optimizing geometric parameters and the ratio of different materials in the *pn* legs, the output power and conversion efficiency of TEGs under large temperature differentials can be significantly improved [23]. Although segmented legs yield superior performance, they may present challenges, given that not all thermoelectric materials exhibit mutual compatibility. When the compatibility factor between two materials diverges by more than 2 units, it becomes arduous to align electrical and thermal fluxes, leading to a substantial decline in efficiency [24].

At the system-level design and engineering, enhancing the heat transfer capacity between the heat source and the TE device through the application of intensified heat transfer principles represents another effective avenue for improving the performance of TEG systems. It is widely recognized that the power generation capability of a TEG hinges on the temperature differential across its two ends [25]. When using gas heat sources for heat energy recovery, given the relatively modest Heat Transfer Coefficient (HTC) within the channels, the heat transfer between the hot fluid and the Thermoelectric Module (TEM) emerges as a crucial determinant of the TEG's performance.

The arrangement of internal heat exchangers plays a crucial role in minimizing the temperature differential between the hot side of the TE device and the hot gas. Commonly employed heat exchanger design methods include the augmentation of heat transfer surface area through finned plates [26,27] or the introduction of pin fins to increase turbulence [28,29]. Chen et al. [25] conducted a study on the performance of TEG systems utilizing low-temperature wastewater and cooling water as hot and cold fluid constituents under various Reynolds numbers. They found that the optimal number of fins was 21 when Re = 10 and 100, while at Re = 1000, the optimal number of fins was 27. Simultaneously, the installation of fins only resulted in a channel pressure drop of less than 1 %. He et al. [30] assessed the impact of the design of plate fin heat exchangers in a heavy-duty diesel engine waste heat recovery TEG on output characteristics. They discovered that the effects of fin spacing and fin height were more significant than fin thickness. Meng et al. [31] employed a fully automated optimization approach to optimize the optimal placement, number, and relative spacing of porous pin fins within the TEG channels, with the goal of increasing output power while reducing pressure drop. The optimal configuration achieved a suitable balance between power and pressure drop, leading to a 22.89 % increase in output power and an 82.98 % reduction in pressure drop. However, the performance enhancement resulting from the installation of fins is limited, as their effectiveness in augmenting heat transfer between the heat source and the TE device is not optimal.

Innovative and highly efficient methods involve the installation of twisted tapes [32] or porous baffles [33] to enhance fluid turbulence within the heat exchanger. In another study, Zhu and colleagues [34] integrated a twisted tape into a ring-shaped TEG with the primary objectives of increasing net power and enhancing the efficiency gain

coefficient. Their study included a comprehensive analysis of how the radius, twist ratio, and length of the twisted tape influenced these performance improvements. Employing a metaheuristic algorithm to optimize these tape parameters resulted in a 10.41 % increase in net power and a 22.51 % improvement in efficiency. Zhao et al. [35] proposed the addition of perforated plates to enhance exhaust heat transfer and studied the impact of inserting perforated plates on thermoelectric performance. The results indicated that when the perforated plates were installed in the optimal position, the output power could increase by 73.4 %. As the perforated plates were positioned closer to the TEG outlet, the voltage uniformity of the TEM first increased and then decreased.

Research has shown that due to the declining temperature of the hot fluid along the length of the TEG, the temperatures on the TEMs also decrease significantly. TEMs located towards the rear of the TEG, closer to the exhaust end, exhibit lower power output compared to modules at the forefront of the system [36]. This is because their temperature gradients are considerably smaller.

A comprehensive approach is to employ metal foam, which not only minimizes thermal resistance between the hot gas and TEM but also enhances temperature uniformity along the TEG [37]. Porous metal foams offer numerous advantages, characterized by a significant surface area and irregular internal framework. When fluid flows through porous metal foam regions, it encounters a large number of random metal frameworks per unit volume, increasing the contact surface area, thereby enhancing nonlinear flow. Furthermore, the elevated thermal conductivity inherent to metals contributes to an amplified heat exchange between the TEM and the metallic foam.

Experimental and simulation-based comparative studies have investigated the heat transfer enhancement effects of two types of heat exchangers: fin-based and metal foam heat exchangers [38]. Under similar operating conditions, it was observed that the thermal resistance of metal foam heat exchangers is approximately halved in comparison to that of conventional heat exchangers [39]. Building upon this insightful conclusion, Lu et al. [40] developed a numerical model for exhaust thermoelectric generators and separately explored the performance of offset rectangular fins and metal foam-enhanced exhaust heat exchangers. Comparative investigations have revealed that, in contrast to offset fins, metal foam exhibits notably higher total power output and energy conversion efficiency. However, it comes at the cost of a more substantial pressure drop, leading to diminished net power, particularly under conditions of elevated exhaust mass flow rates. Wang et al. [41] undertook a comprehensive investigation into the influence of metal foam inserts featuring diverse porosities on thermoelectric waste heat recovery systems. Their findings indicated that the utilization of 5 PPI (pores per inch) metal foam led to a noteworthy enhancement in the maximum electrical generation efficiency of the TEG, amounting to 2.05 %, marking a substantial increase of 29.75 % compared to the non-filled TEG. Nonetheless, it's worth noting that as the flow rates increased, the pressure drop exhibited an exponential growth trajectory. Nithyanandam et al. [42] provided a detailed numerical simulation demonstrating the enhancing effects of metal foam on TEG power density and net power. The maximum net power produced with metal foam configurations was 5.7–7.8 times that of configurations without metal foam, underscoring the superior performance of metal foams. Li et al. [43] established an experimental platform for a thermoelectric power generation system based on metal foam heat exchangers and analyzed the impact of different foam insertion methods in the central flow area. The results indicated that porous foam copper with a thickness of 15 mm, a porosity of 20 PPI, and a 75 % fill rate exhibited the best overall performance. However, all of the mentioned studies pointed out that the pressure drop associated with porous foam is substantial.

To address this challenge, some have proposed that achieving higher heat transfer coefficients within an acceptable pressure drop range is possible by employing different pore structures and component distributions [44,45]. While this presents a promising prospect, it is imperative to acknowledge that the impact of gradient metal foam structures on the holistic performance of thermoelectric generators has not yet been thoroughly investigated through simulations or empirical experimentation.

1.2. Motivation and innovation

A foremost challenge in waste heat recovery and power generation applications is the notably low efficiency of heat transfer between the hot fluid and TEMs. This is precisely why the introduction of metal foams in TEGs has gained prominence, aiming to achieve optimal performance in forced-convection heat transfer. Metal foams excel in this regard relative to traditional fins or disturbance tapes, owing to their superior heat transfer enhancement capabilities. Nevertheless, the effective utilization of metal foams in TEGs continues to face challenges related to high pressure drop and parasitic power loss, necessitating comprehensive performance assessments and innovative configuration optimization studies to provide design guidance for metal foam TEG manufacturing.

To address this challenge, this study introduces a novel approach involving axial gradient metal foam with varying pore density/porosity along the direction of the fluid flow. This approach is aimed at achieving high TEG power output while circumventing high pressure drop and parasitic power losses, representing the innovation in this research.

Given the high processing and production costs of heat exchangers and thermoelectric modules, most researchers currently favor theoretical modeling methods to optimize TEG systems, rather than creating multiple physical models with varying parameters and comparing their performance through experimental testing [46]. Consequently, this study employs a logical closed-loop approach consisting of mathematical modeling, model validation, numerical optimization, and experimental verification to conduct efficient TEG optimization research.

The research establishes an analytical model for a waste heat thermoelectric power generation system incorporating gradient metal foams. A prototype is manufactured and tested to validate the analytical model. Subsequently, the study investigates the impact of critical structural parameters of metal foams on thermoelectric performance and employs numerical methods to optimize the gradient foam structure within the exhaust flow channels. Finally, the experimental prototype is used to conduct experimental research and comparative validation against the numerical optimization results.

2. Mathematical model and formulation description

2.1. Model development and assumptions

A typical thermoelectric generator comprises three main components: thermoelectric modules, a heat source heat exchanger, and a cold side heat exchanger. Fig. 1 provides an illustrative diagram of the TEG system, gradient metal foam heat exchanger, and TEM model adopted in this study. To enhance the exhaust heat transfer capacity while maintaining low pressure drop, a gradient metal foam heat exchanger has been proposed. The exhaust heat exchanger is divided into three heat transfer regions in the direction of fluid flow. Metal foam with different PPI (or porosity) is embedded within each region of the core flow field. Fig. 1(c) presents an example with an increasing gradient of PPI. The dimensions of the aluminum alloy heat exchanger are 320 mm in length, 120 mm in width, 20 mm in height, and 1.5 mm in wall thickness.

The structure of metal foam is primarily characterized by its porosity and PPI, which represent the void volume as a ratio of the total metal foam volume and the number of pores within a 25.4 mm length, respectively. Another significant geometric parameter is the surface area per unit volume, which can be obtained from manufacturer data. Additionally, fiber thickness influences the heat transfer efficiency of metal foam. As shown in Table 1, samples with PPI values of 5, 10, 20, and 40, and porosities ranging from 0.90 to 0.96 were studied [38].

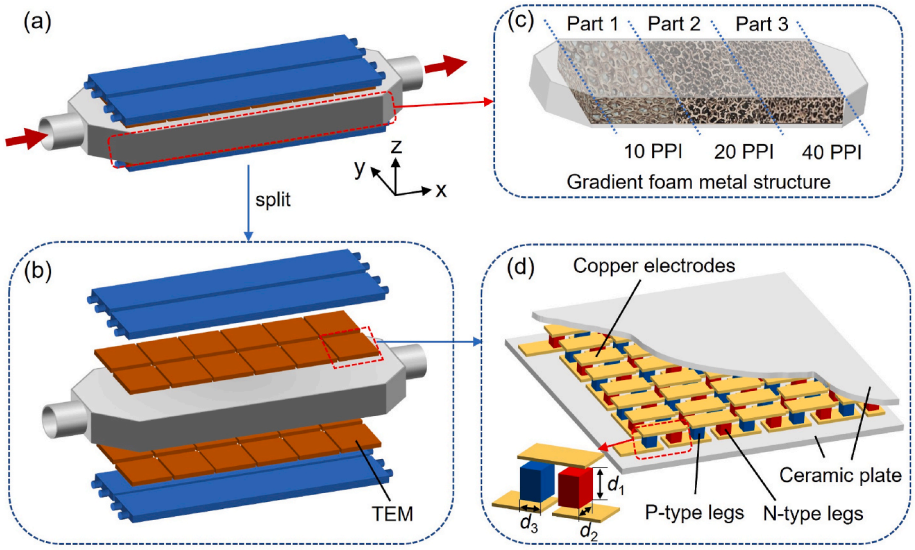

Fig. 1. Architecture of the metal foam thermoelectric generator. (a) Integration diagram of the TEG. (b) Split diagram of the TEG. (c) Gradient metal foam heat exchanger. (d) Thermoelectric module and thermoelectric legs.

Table 1
Structural parameters of metal foams.

Name	Sample	PPI (in^{-1})	Porosity, ω	Area per unit of volume, a_{sv} (m^3 m^{-2})	Fiber thickness, $t \times 10^{-3}$ (m)	Permeability, $\phi \times 10^7$ (m^2)	Inertia Coeff., g
MF1 (5–0.93)	Al-5-8.0	5	0.93	342	4.90	1.52	0.059
MF2 (10–0.96)	Al-10-4.6	10	0.96	554	3.85	2.165	0.108
MF3 (10–0.93)	Al-10-7.4	10	0.93	736	5.53	4.29	0.129
MF4 (10–0.90)	Al-10-10.4	10	0.90	866	4.84	2.65	0.106
MF5 (20–0.93)	Al-20-7.0	20	0.93	1169	3.15	0.535	0.050
MF6 (40–0.93)	Al-40-7.4	40	0.93	1721	2.82	0.297	0.050

Pressure drop calculations for metal foam were conducted according to recommendations from publicly available literature [38]. Permeability (ϕ) and inertia coefficients (f) for the aforementioned metal foam models were estimated based on experimental data [39]. According to the supplier, the solid-phase effective conductivity of aluminum foam is 3.4 W/(m K). All six metal foam samples are 100 mm in length, 100 mm in width, and 20 mm in height.

In the heat exchanger, 24 commercial $B_{i2}Te_3$-based thermoelectric modules (TEG1-19913, Hubei Sagreon New Energy Technology Co., LTD) are adhered to the upper and lower surfaces and connected in series. Each individual module has a dynamic internal resistance of 2.8 Ω. Fig. 1(d) presents a simplified schematic of a single thermoelectric module. In contrast to other studies, large surface area power generation modules were chosen, with dimensions of 50 mm in length, 50 mm in width, and 3.7 mm in height. Each TEM contains 198 pairs of *pn* legs, and the dimensions of an individual semiconductor leg are 1.4 mm in length, 1.4 mm in width, and 1.0 mm in height. The outer sides of the thermoelectric modules are outfitted with four aluminum alloy cooling heat exchangers. Each heat exchanger measures 300 mm in length, 50 mm in width, and 12 mm in height, with a thickness of 1.5 mm. Every six TEMs are covered by a cooling pipeline.

Based on the physical model described in Fig. 1, we have established a mathematical model for the exhaust TEG system filled with gradient metal foam. Fig. 2(a) illustrates the heat transfer inside the TEG, depicting the variation in hot fluid temperature and cooling water temperature along the flow direction. As shown in Fig. 2(b), in the *x*-*y*

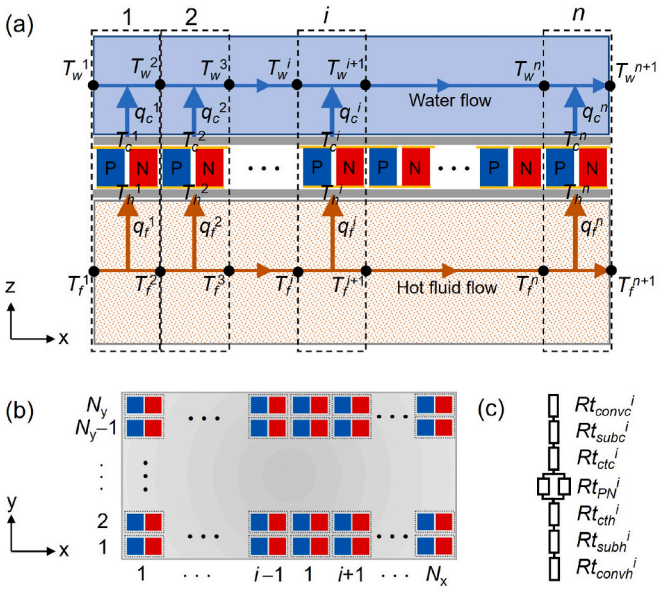

Fig. 2. Modeling of the TEG. (a) Finite element model of the metal foam thermoelectric generator. (b) Numbering for thermoelectric legs. (c) Equivalent thermal resistance of a couple of thermoelectric leg.

direction, the surface of one side of the heat exchanger covering the thermoelectric modules can be represented by $N_x \times N_y$ based on the total number of thermoelectric legs. Considering that *pn* legs in the *y*-direction exhibit similar temperature and flow velocity field distributions, each row of *pn* couples in the *y*-direction is taken as a calculation unit, thus dividing the entire TEG into $n = N_y$ calculation units. For the *i*-th (i = 1 to n) calculation unit, the hot fluid and cooling fluid flow in with temperatures T_f^i and T_w^i, respectively. The heat released by the hot fluid is transferred to the *pn* leg's hot end surface, causing the temperature to rise to T_h^i. The temperature at the cold end surface of the *pn* leg is T_c^i. When connected to an external load R_L, the TEM directly converts the heat energy into electrical energy with a working temperature difference of $\Delta T^i = T_h^i - T_c^i$. Fig. 2(c) depicts the thermal resistance model of a couple of thermoelectric leg, primarily encompassing the thermal resistance on the *pn* couple (Rt_{pn}), substrate layer (Rt_{sub}), convective heat resistance (Rt_{conv}), and contact resistance (Rt_{ct}).

The complex modeling problem has been simplified based on the following assumptions: (1) the gap between the thermoelectric legs and the sides of the heat exchanger are adiabatic; (2) natural convection and thermal radiation are neglected; (3) the system is considered to be in a steady state; (4) fluid flow distribution is assumed to be uniform along the axial direction at any given cross-section; (5) the impact of the Thomson effect is disregarded.

2.2. Governing equations

Within the *i*-th calculation unit, the heat transfer rates at the hot end (q_h^i) and cold end (q_c^i) of the thermoelectric legs can be expressed in three different forms: The first form represents the sum of heat flux rates resulting from the Peltier effect, Fourier effect, and Joule effect. The second form accounts for the external irreversibilities due to finite heat transfer rates, determined according to Newton's cooling law. The third form represents the heat released or absorbed by the heat exchanger in terms of the enthalpy difference before and after the fluid flows through the pipeline, in accordance with the law of energy conservation. The heat transfer rates at the hot and cold ends are described by these three expressions, considering various heat transfer mechanisms and conservation laws.

$$\begin{cases} {q_h}^i = N_y\left[{\alpha_{pn}}^i I T_h^i + {K_{pn}}^i\left(T_h^i - T_c^i\right) - 0.5I^2{R_{pn}}^i\right] \\ {q_c}^i = N_y\left[{\alpha_{pn}}^i I T_c^i + K_{pn}^i\left(T_h^i - T_c^i\right) + 0.5I^2 R_{pn}^i\right] \end{cases} \tag{1}$$

$$\begin{cases} {q_h}^i = N_y k_f S\left(\dfrac{T_f^i + T_f^{i+1}}{2} - T_h^i\right) \\ {q_c}^i = N_y k_w S\left(T_c^i - \dfrac{T_w^i + T_w^{i+1}}{2}\right) \end{cases} \tag{2}$$

$$\begin{cases} {q_h}^i = 0.5 m_f c_{pf}\left(T_f^i - T_f^{i+1}\right) \\ {q_c}^i = 0.5 m_w c_{pw}\left(T_w^{i+1} - T_w^i\right) \end{cases} \tag{3}$$

The series current of TEM is expressed as:

$$I = \left(\sum_{i=1}^{N_x} N_y {\alpha_{pn}}^i \Delta T^i\right) \Big/ \left(R_L + N_y \sum_{i=1}^{N_x} {R_{pn}}^i\right) \tag{4}$$

In accordance with the physical model constructed based on Fig. 1, the total output power is obtained by subtracting the heat absorbed on the hot side from the heat released to the radiator on the cold side. This calculation involves both the upper and lower parts of the heat exchanger. Therefore, the calculation of the TEG's output power is given as:

$$P = 2\sum_{i=1}^{N_x}\left({q_h}^i - {q_c}^i\right) \tag{5}$$

Where α_{pn}^i, K_{pn}^i, and R_{pn}^i represent the average Seebeck coefficient, thermal conductivity, and electrical resistance of the *pn* couple in the *i*-th calculation unit, and k_f and k_w denote the total HTC at the hot and cold ends. They are specifically defined as follows:

$${\alpha_{pn}}^i = \left[\int_{T_c^i}^{T_h^i} \alpha_p(T)dT - \int_{T_c^i}^{T_h^i} \alpha_n(T)dT\right] \Big/ \Delta T^i \tag{6}$$

$${K_{pn}}^i = d_2 d_3\left(\int_{T_c^i}^{T_h^i} \lambda_p(T)dT + \int_{T_c^i}^{T_h^i} \lambda_n(T)dT\right) \Big/ d_1 \Delta T^i \tag{7}$$

$${R_{pn}}^i = d_1\left(\int_{T_c^i}^{T_h^i} \rho_p(T)dT + \int_{T_c^i}^{T_h^i} \rho_n(T)dT\right) \Big/ d_2 d_3 \Delta T^i \tag{8}$$

$$k_f = 1 \Big/ \left(1/h_f + Rt_{sub,h} + Rt_{con,h}\right) \tag{9}$$

$$k_w = 1 \Big/ \left(1/h_w + Rt_{sub,c} + Rt_{con,c}\right) \tag{10}$$

Where $\alpha(T)$, $\lambda(T)$, and $\rho(T)$ denote the temperature-dependent curves of the physical properties of *p* or *n*-type semiconductors [47]. The contact thermal resistance, Rt_{con}, can be assumed to be 0.0005 m^2K/W [14]. The thermal resistance of the substrate layers on both the hot and cold sides is symmetric, consisting of copper plates, ceramic plates, and thermal resistance on the heat exchanger walls, and can be expressed as:

$$Rt_{sub} = \delta_{cu}/\lambda_{cu} + \delta_{ce}/\lambda_{ce} + \delta_{hex}/\lambda_{hex} \tag{11}$$

For the coolant pipes, the convective HTC within the cooling pipe is given as:

$$h_w = \left(Nu_w \lambda_w\right) / D_{hy} \tag{12}$$

Under conditions of fully developed turbulent flow, the Nusselt number and Reynolds number for water within the cooling pipes can be calculated as [40]:

$$Nu_w = \frac{Pr_w f_w (Re_w - 1000)\left[1 + \left(D_{hy}/L_{hex}\right)^{2/3}\right]}{8\left[1 + 12.7\left(Pr_w{}^{2/3} - 1\right)\sqrt{f_w/8}\right]} \qquad Re_w = 2300 - 10^6, Pr_w = 0.6 - 10^5 \tag{13}$$

$$Re_w = v_w D_{hy} \varepsilon_w / \mu_w \tag{14}$$

$$f_w = \left[1.82\ln(Re_w) - 1.64\right]^{-2} \tag{15}$$

Where v_w, ε_w, and μ_w represent the velocity, density, and dynamic viscosity coefficient of the cooling water, respectively. Pr_w, Re_w, and f_w represent the Prandtl number, Reynolds number, and friction factor of the cooling water, respectively. L_{hex} represents the length of the heat exchanger, and in this model, the lengths of the hot and cold-side heat exchangers are the same.

Due to the complex geometric shape of the metal foam, detailed flow data cannot be obtained through experiments. Typically, only macroscopic quantities can be measured. For a smooth flat plate heat exchanger filled with metal foam, the HTC of the metal foam is estimated based on a simplified model proposed and experimentally validated by Mancin et al. [38].

$$h_f = \Omega H_{hex} \Phi a_{sv}/2 \tag{16}$$

Where a_{sv} represents the surface area per unit volume of the metal foam. This model is applicable under fully developed turbulent flow conditions, as outlined in Table 1 for the foam metal samples.

The interstitial HTC of the metal foam, Φ, is expressed as:

$$\Phi = \begin{cases} 0.058 Re_f^{0.75} Pr_f^{1/3} \Big/ t, \text{PPI} = 5 \\ 0.02 Re_f^{0.9} Pr_f^{1/3} \Big/ t, \text{PPI} \geq 10 \end{cases} \tag{17}$$

Where t represents the fiber thickness.

The Reynolds number inside the heat exchanger, Re_f, is calculated as:

$$Re_f = m_f t \Big/ \left(H_{hex} W_{hex} \mu_f \omega \right) \tag{18}$$

Where μ_f represents the dynamic viscosity coefficient of the heat fluid, H_{hex} and W_{hex} represent the height and width of the heat exchanger, and ω denotes the porosity of the metal foam. In general, for extended heat transfer surfaces, the overall efficiency (Ω) can be expressed as:

$$\Omega = \frac{1 + 0.5 a_{sv} H_{hex} \tanh\left(l_{mf} \sqrt{4\phi/\lambda_{mf} t}\right) / l_{mf} \sqrt{4\phi/\lambda_{mf} t}}{1 + 0.5 a_{sv} H_{hex}} \tag{19}$$

The equivalent fin length (l_{mf}) is expressed as:

$$l_{mf} = 6.6 \text{PPI}^{0.99} H_{hex} (0.0254 - t\text{PPI}) \tag{20}$$

The calculation of the pressure drop incurred during forced convection of the fluid through the metal foam-equipped heat exchanger is [48]:

$$\Delta P = \left(\varepsilon_f \mu_f v_f \Big/ \phi + \varepsilon_f g \mu_f^2 \Big/ \sqrt{\phi} \right) L_{hex} \tag{21}$$

Where ϕ and g represent the permeability and inertia coefficient, respectively.

The non-uniformity in the output voltage of various positions on the TEG is bound to result in an inevitable parasitic power loss when all the thermoelectric modules are interconnected. The coefficient of voltage uniformity can serve as a metric to assess the impact of output non-uniformity on TEG performance and is defined as follows:

$$\gamma = 1 - \sum_{i=1}^{N_x} \frac{\sqrt{\left(N_y \alpha_{pn}^i \Delta T_i - P \Big/ N_x I \right)^2}}{N_x I} \tag{22}$$

The thermal-to-electric conversion efficiency (η_{te}) of a TEG can be calculated as the ratio of the output power to the actual heat extraction rate:

$$\eta_{te} = P \Big/ \sum_{i=1}^{Nx} {q_h}^i \tag{23}$$

The heat recovery efficiency (η_{hr}) of the heat exchanger and TEG is calculated as the percentage of the actual energy extraction rate to the maximum possible energy extraction rate.

$$\eta_{te} = \sum_{i=1}^{Nx} {q_h}^i \Big/ m_f c_{pf} \left(T_f^1 - T_a \right) \tag{24}$$

Where T_a is the ambient temperature.

2.3. Solution process

A MATLAB program has been developed for solving the aforementioned system of equations. Constants are established based on the constructed physical model and the structural parameters of the TEG. The boundary conditions for the model are the temperatures (T_f^1 and T_w^1) and mass flow rates (m_f and m_w) at the entry of the first computational unit for the hot fluid and cooling water, respectively. The physical properties of the thermoelectric semiconductor exhibit significant temperature dependence, as detailed in Table 2. Given the substantial temperature variation as the hot fluid passes through the TEG, the dynamic viscosity, thermal conductivity, density, and specific heat capacity are determined as temperature-dependent functions. The fluid parameters employed in this model are listed in Table 3.

Table 2
Physical properties of the TEM.

Component	Property	Value	Units
Copper Electrodes	Thermal conductivity, λ_{cu}	398	W m^{-1} K^{-1}
	Thickness, δ_{cu}	0.00035	m
Ceramic	Thermal conductivity, λ_{ce}	35	W m^{-1} K^{-1}
	Thickness, δ_{ce}	0.0008	m
Heat exchanger	Thermal conductivity, λ_{hex}	204	W m^{-1} K^{-1}
	Thickness, δ_{hex}	0.0015	m
P-type leg [14]	Seebeck coefficient, $\alpha_p(T)$	$1.61 \times 10^{-4} - 1.818 \times 10^{-6} T + 1.11 \times 10^{-8} T^2 - 2.035 \times 10^{-11} T^3 + 1.134 \times 10^{-14} T^4$	V K^{-1}
	Resistivity, $\rho_p(T)$	$-5.01 \times 10^{-5} + 3.519 \times 10^{-7} T - 7.74 \times 10^{-10} T^2 + 8.94 \times 10^{-13} T^3 - 4.32 \times 10^{-16} T^4$	Ω m
	Thermal conductivity, $\lambda_p(T)$	$-46.97 + 0.457T - 1.575 \times 10^{-3} T^2 + 2.331 \times 10^{-6} T^3 - 1.242 \times 10^{-9} T^4$	W m^{-1} K^{-1}
N-typse leg [14]	Seebeck coefficient, $\alpha_n(T)$	$-4.428 \times 10^{-4} + 3.469 \times 10^{-6} T + 1.42 \times 10^{-8} T^2 + 2.325 \times 10^{-11} T^3 - 1.3 \times 10^{-14} T^4$	V K^{-1}
	Resistivity, $\rho_n(T)$	$-8.072 \times 10^{-6} + 4.507 \times 10^{-8} T + 7.827 \times 10^{-11} T^2 - 2.305 \times 10^{-13} T^3 + 1.317 \times 10^{-16} T^4$	Ω m
	Thermal conductivity, $\lambda_n(T)$	$10.12 - 7.414 \times 10^{-2} T + 2.246 \times 10^{-4} T^2 - 3.019 \times 10^{-7} T^3 + 1.537 \times 10^{-10} T^4$	W m^{-1} K^{-1}

The flat-plate heat exchanger is subdivided into three segments, each filled with metal foam materials having distinct structural parameters. Consequently, this model computes the average HTCs for the thermal cores of the three metal foams separately. For the overall model solution, the process begins by initially predicting a value for the total series current, denoted as I_0, along with the initial hot-side HTC, k_{f0}, and the cold-side HTC, k_{w0}. Utilizing Eqs. (1)–(3), the model computes the temperature distribution of the TEG within the first filled region, as well

Table 3
Physical properties of working fluid.

Fluid	Property	Value	Units
Exhaust gas [46]	Specific heat capacity, $c_{p,f}$	$1.0731 - 5.7059 \times 10^{-4} T + 1.4411 \times 10^{-6} T^2 - 1.0838 \times 10^{-9} T^3 + 2.8163 \times 10^{-13} T^4$	kJ kg^{-1} K^{-1}
	Density, ε_f	$3.1589 - 1.051 \times 10^{-2} T + 1.6237 \times 10^{-5} T^2 - 1.1708 \times 10^{-8} T^3 + 3.178 \times 10^{-12} T^4$	kg m^{-3}
	Thermal conductivity, λ_f	$-1.817 \times 10^{-3} + 1.08 \times 10^{-4} T - 5.238 \times 10^{-8} T^2 + 1.4149 \times 10^{-11} T^3$	W m^{-1} K^{-1}
	Dynamic viscosity, μ_f	$2.68 \times 10^{-6} + 6.098 \times 10^{-8} T - 2.8219 \times 10^{-11} T^2 + 7.005 \times 10^{-15} T^3$	Pa s
	Mass flow rate, m_f	0.01–0.05	kg s^{-1}
	Inlet temperature, T_f^1	523–623	K
Cooling water [30]	Specific heat capacity, $c_{p,w}$	4.177	kJ kg^{-1} K^{-1}
	Density, ε_w	9.981×10^{-5}	kg m^{-3}
	Dynamic viscosity, μ_w	5.494×10^{-4}	Pa s
	Thermal conductivity, λ_w	0.59	W m^{-1} K^{-1}
	Mass flow rate, m_w	0.167	kg s^{-1}
	Inlet temperature, T_w^1	313	K

as the average HTCs $k_f(1)$ and $k_w(1)$ for that section. If the current heat transfer coefficients differ from the initial predictions, an adjustment is made to the predicted values and recalculations are carried out until they converge. Following this, the fluid parameters at the outlet of the first filled region ($T_f^{Nx/3}$, $T_w^{Nx/3}$, m_f, and m_w) serve as the input parameters for the second filled region, and the previous steps are repeated. The same procedure applies to the third filled region. Finally, the model obtains the complete temperature distribution of the TEG. Due to the decrease in exhaust temperature and the increase in cooling water temperature, this temperature distribution will demonstrate a trend of gradually decreasing temperature difference along the direction of exhaust gas flow across the thermoelectric legs. Then, the new electric current I is calculated based on Eq. (4). If I differs from I_0, adjustments are made to the predicted value I_0 and recalculations are conducted until I and I_0 align. The computational workflow is depicted in Fig. 3.

3. Experimental system and parameters calculation

3.1. Experimental test rig

In order to assess the thermoelectric performance of the TEG system based on gradient metal foam heat exchangers and validate the reliability of the established mathematical model, an experimental setup has been constructed. This setup includes a detachable metal foam heat exchanger.

The experimental apparatus comprises four main units: a heat source simulation unit, a TEG unit, a cooling unit, and a measurement/data acquisition unit, as depicted in Fig. 4. According to the physical model described in Section 2.1, plate-type heat exchangers and cooling water pipelines of identical dimensions, capable of accommodating metal foam, were designed and fabricated. A total of 24 thermoelectric modules are uniformly arranged on the heat exchanger's hot end surface. To minimize thermal resistance, each side of the TEMs is coated with thermally conductive silicone grease. The cold-end heat exchanger is tightly fastened to the exhaust heat exchanger using bolts. At the segments of the heat exchanger, grooves are uniformly provided to facilitate the stable fixation of the metal foam. The height of the metal foam matches that of the heat exchanger channels, ensuring close contact between the metal foam and the wall surface.

To enable the TEG system to operate under stable inlet flow rate and temperature conditions, an industrial hot air blower (RY-P-15A-075, Junre Machinery Equipment Co., LTD) was employed as a simulated heat source in lieu of an automobile engine to provide high-temperature hot fluid. The high-temperature air blower boasts a maximum power of 15 kW, and the output temperature can be precisely controlled within the span of 0–633 K using a PID controller. Simultaneously, it offers the flexibility to adjust the exhaust flow rate within the range of 0–240 m^3/h via the control panel while maintaining the presence of high-temperature gases. To measure the actual exhaust flow rate, temperature, and heat exchanger outlet pressure, a vortex flowmeter (HW-LUGA14, Walv Control Technology Co., LTD) was positioned at the heat exchanger's outlet, powered by a 24V DC power supply system (DP832, RIGOL Technologies Co. LTD). Within a full range of 50–480 m^3/h, the vortex flowmeter exhibits an accuracy of ±1 %.

The hot fluid passes through the TEG and the vortex flowmeter before being discharged from the pipe at standard atmospheric pressure. The inlet pressure of the TEG is measured by a manometer integrated at the outlet of the industrial blower, while the outlet pressure is directly measured by a vortex flowmeter. Based on these measured data, the pressure drop of the TEG is calculated. The air blower, TEG modules, and vortex flowmeter are connected via stainless steel pipes with flanges. We have covered aerogel felt on the outer wall and joints of the connecting pipes to reduce heat loss. In order to ensure efficient cooling fluid circulation and the consistent maintenance of a stable temperature on the cold side, we employed a circulating water vacuum pump (SHZ-95B, Shanghai Yuhua Instrument Equipment Co., LTD). This pump facilitated heat dissipation with a cooling fluid flow rate of approximately 10 L/min, thereby generating a steady water mass flow rate of 0.167 kg/s. The water tank serves as a thermal energy reservoir. The radiator is connected to the cooling water channel, where water is drawn from a 57 L

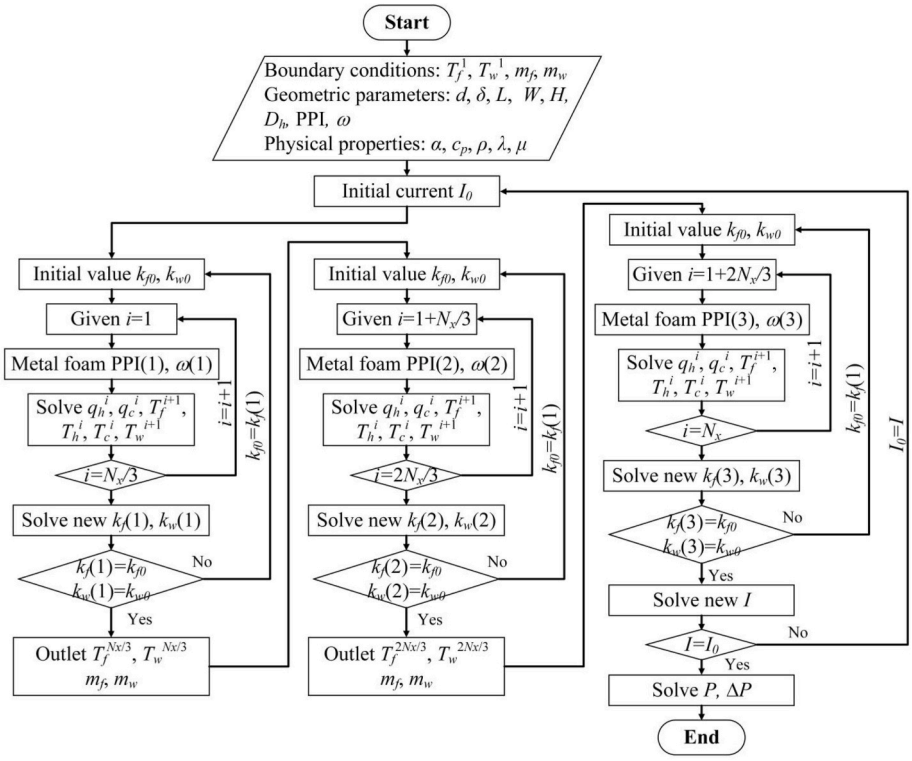

Fig. 3. Solution process.

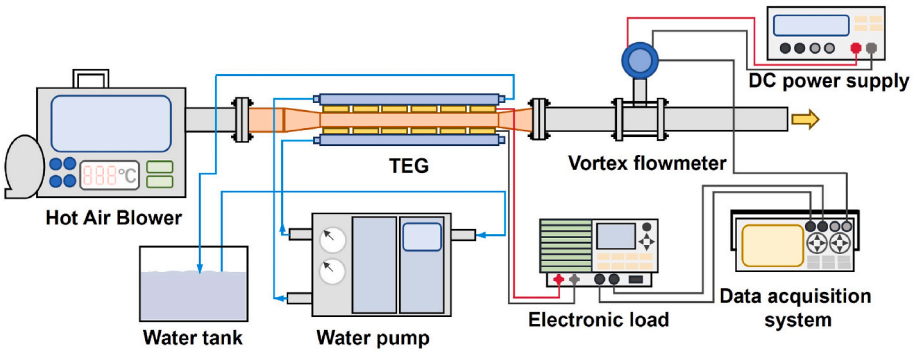

Fig. 4. Experimental system of thermoelectric generator.

capacity water tank and pumped into the cooling water pipes. It flows through the TEG and returns to the water tank, ensuring a continuous circulation process facilitated by a water pump. Due to the large water tank capacity, the time required to reach a stable output when starting the generator during the experimental process is brief, ensuring a consistent cooling water temperature.

To evaluate the output performance across various load resistances, the thermoelectric modules are connected to an electronic load (Array 3721A, Array Electronics Co., LTD). In constant resistance mode, the load resolution is 0.1 mΩ, with full-scale accuracy of ±0.5 %. Experimental data is monitored and collected using a data acquisition device (DSO-X 2024A, Agilent Technologies Co. LTD).

Steady-state conditions are considered achieved if the temperature variation at the TEG outlet remains within ±0.1 K for a continuous 5-min period under a fixed operating condition of the hot air blower. Current-voltage data are collected across the TEG output by scanning the load resistance from 10 to 100 Ω, and output power is calculated based on these values. The blower is directly connected to the TEG, with the blower outlet and TEG inlet having identical structures and a very short distance between them, resulting in minimal pressure drop. Therefore, the mass flow rate at the blower outlet is considered to be the same as the speed at the TEG inlet. The pressure at the outlet of the TEG is directly measured by the vortex flowmeter. Additionally, a pressure sensor is installed at the TEG inlet, allowing the calculation of the pressure drop across the TEG by taking the difference between the outlet pressure and the inlet pressure.

3.2. Model validation

To validate the accuracy of the established mathematical model, experiments were conducted under conditions of an inlet temperature of 573 K and a fixed mass flow rate of 0.03 kg/s, examining the TEG output performance at various load resistances. The flow channel of the flat-plate heat exchanger was filled with porous metal aluminum foam (Al-10-4.6) with a porosity of 0.96 and a PPI of 10. Fig. 5(a) provides a comparison between simulated predictions and experimental results for total output power under different load resistances. The predicted output power aligns closely with the experimental data. The maximum deviation between the simulation and experimental data is 8.97 %, with an average deviation of 4.85 %. Furthermore, the model proposed for load resistances in the range of 50–80 Ω exhibits a strong fit with experimental data.

The model's predictive performance regarding fluid resistance characteristics was also evaluated. Fig. 5(b) illustrates the impact of mass flow rate on pressure drop in the metal foam heat exchanger at different inlet temperatures. It is observed that the pressure drop sharply increases with higher mass flow rates, while the effect of inlet temperature on pressure drop is relatively minor. The numerical results display slight variances in comparison to experimental findings, with the highest deviation remaining below 7 %, which falls within an acceptable margin.

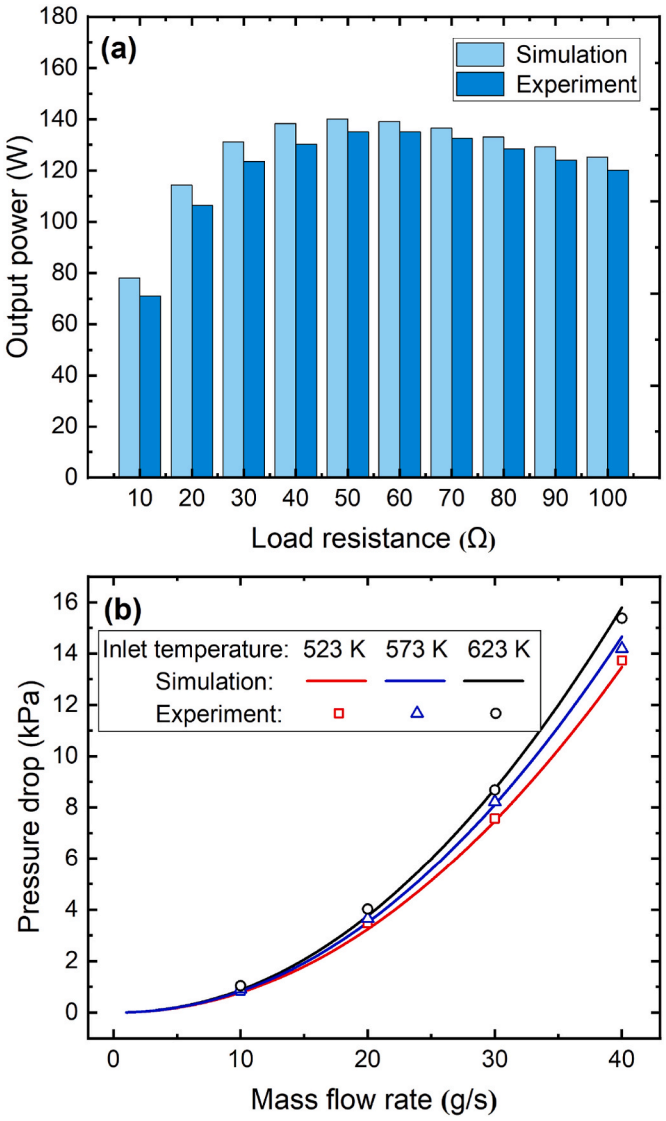

Fig. 5. Model validation. (a) Experimental and simulation comparison of electric power output vs. load resistance. (b) Experimental and simulation comparison of pressure drop vs. mass flow rate.

Experimental evaluations of TEG output characteristics and flow resistance characteristics indicate that the established mathematical model demonstrates good effectiveness and can be employed for further analysis. The differences between experimental results and numerical

simulations can primarily be attributed to three factors: 1) discrepancies in contact thermal resistance and contact resistance between simulation and experimentation; 2) measurement inaccuracies in the experimental setup; 3) simplifications in the theoretical model.

4. Numerical results

4.1. Influence of metal foam on thermoelectric performance

Forced convection heat transfer within metal foam is closely intertwined with the structural properties of the foam itself. Variations in pore density and porosity result in differences in pore size and fiber diameter within the metal foam, thereby giving rise to distinct heat transfer and flow characteristics of the fluid within the metal foam. In this section, numerical methods will be employed to explore the impact of critical structural parameters of the metal foam on TEG performance.

4.1.1. Pore density

Under the condition of an inlet temperature of 573 K, an analysis was conducted to examine the impact of metal foam pore density on TEG output power and HTC at different mass flow rates, as depicted in Fig. 6 (a). Here, the porosity of the metal foam was kept constant at 0.93.

Both output power and HTC increase with rising mass flow rates and higher pore density. As pore density increases, the surface-to-volume ratio of metal foam fibers grows, intensifying heat dispersion. Simultaneously, internal fluid disturbance increases, thinning the gas boundary layer, and enhancing turbulence within the heat exchanger, thereby promoting heat transfer between gas and solid phases. This results in an elevation of the HTC on the metal foam and an increase in the hot-side wall temperature of the TEG, ultimately enhancing the output power.

Fig. 6(b) illustrates the influence of metal foam pore density on TEG's voltage uniformity and pipeline pressure drop. At any given mass flow rate, the voltage uniformity coefficient decreases with increasing PPI of the metal foam. This is due to the metal's significantly higher thermal conductivity compared to air, and the increase in pore density signifies a reduction in pore size. With a consistent porosity, the solid dimensions of the metal foam shrink accordingly, leading to an increase in the specific surface area of the gas-solid interface, and stronger gas disturbance within the pipeline [43]. Unlike smooth pipe heat exchangers, the fluid flow within metal foam pipes becomes more uniform, and the temperature gradient in the gas flow direction increases, resulting in significantly higher temperatures at the upstream wall surface of the heat exchanger compared to the downstream wall surface [49]. Greater PPI intensifies this effect. The distribution of voltage in TEMs is influenced by the working temperature difference at their specific locations. Consequently, voltage uniformity decreases with the increase in PPI. However, increasing mass flow rates can mitigate the effect of varying pore density on voltage uniformity.

As per Fig. 6(b), pressure drop exhibits exponential growth as mass flow rates increase. The solid structure dimensions of metal foam expand significantly with the increase in pore density, resulting in a noticeable rise in inlet and outlet pressure drops for TEG. Particularly, after increasing pore density from 10 PPI to 20 PPI or higher, a complex and random solid framework severely impedes fluid flow, significantly amplifying the pressure drop.

As depicted in Fig. 6(c), the trend of the TEG's thermal-electric efficiency follows the output power, whereas the heat recovery efficiency decreases with the increase in mass flow rate. Increasing PPI can enhance the heat extraction rate, attributed to the intensified convective heat transfer facilitated by the high turbulence induced by high PPI metal foam, enhancing the heat transfer at the wall surface.

4.1.2. Pore porosity

Furthermore, under the same boundary conditions, an analysis was conducted to assess the impact of metal foam porosity on TEG thermoelectric performance at different mass flow rates, as illustrated in Fig. 7. In this case, the metal foam pore density was kept constant at 10 PPI, while the porosity ranged from 0.9 to 0.96. Contrary to pore density, increasing porosity leads to a reduction in HTC, output power, thermoelectric efficiency, and pipeline pressure drop while enhancing voltage uniformity and heat recovery efficiency. This is because the influence of increased porosity on the metal foam structure is inverse to that of pore density. A higher porosity implies a reduction in the metal skeleton and an enlargement of the fluid flow region within the metal foam, thus diminishing fluid disturbance. The foam with the lowest porosity and the highest relative density (Al-10-9.7) exhibits the highest overall heat transfer coefficient.

4.2. Influence of gradient metal foam on thermoelectric performance

The addition of metal foam can enhance heat transfer at the hot end, thereby contributing to improved thermoelectric performance. However, it also significantly increases pressure drop within the pipeline. When applying such metal foam-filled TEGs for automotive engine waste heat recovery, the resulting exhaust backpressure can have adverse effects on the engine [50]. To mitigate the negative impact of this added pressure drop, we partially fills the pipeline with gradient metal foam (GMF), aiming to simultaneously achieve high thermoelectric performance and low pressure drop.

4.2.1. Gradient pore density

Gradient metal foam refers to the insertion of metal foam with different pore sizes at various sections within the heat exchanger. For instance, as depicted in Fig. 1(c), the designation "10-20-40 PPI" for the sample denotes the arrangement of metal foam, with the lower-porosity foam (10 PPI) situated at the inlet, followed by the intermediate-porosity foam (20 PPI), and concluding with the higher-porosity foam (40 PPI) near the outlet. This configuration, where the metal framework density increases along the fluid flow direction, is referred to as the positive gradient direction. The composition of the 40-20-10 PPI sample is identical to that of the 10-20-40 PPI sample, but the placement is reversed, defining it as the negative gradient direction. In our definition,

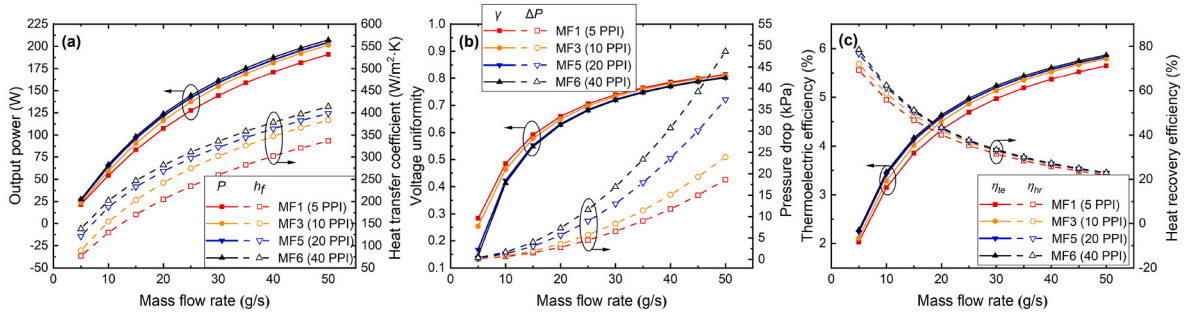

Fig. 6. Effects of exhaust mass flow on (a) output power and heat transfer coefficient, (b) voltage uniformity coefficient and pressure drop, and (c) thermoelectric efficiency and heat recovery efficiency at different pore densities.

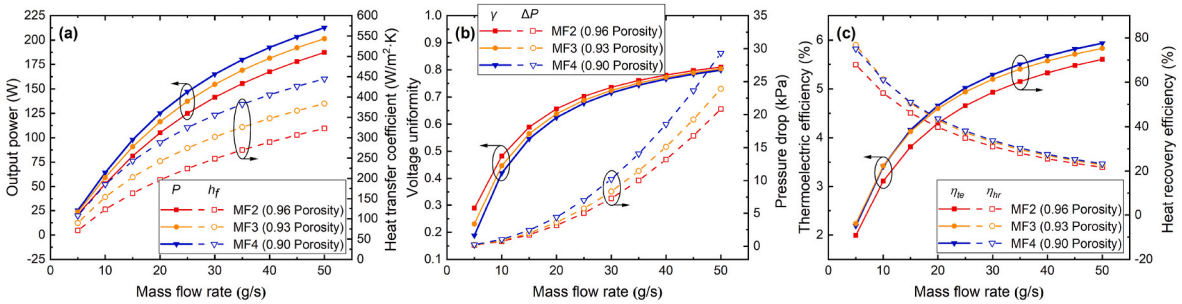

Fig. 7. Effects of exhaust mass flow on (a) output power and heat transfer coefficient, (b) voltage uniformity coefficient and pressure drop, and (c) thermoelectric efficiency and heat recovery efficiency at different porosity.

a positive gradient signifies an increase in metal framework dimensions along the direction of fluid flow, whereas a negative gradient indicates the opposite. The filling rate of metal foam within the pipeline is defined as the ratio of the total volume of the metal foam to the total volume of the channel.

Initially, by keeping the metal foam structure fixed and altering the height of the heat exchanger, the impact of the metal foam filling rate on thermoelectric performance was investigated. Fig. 8 illustrates the influence of filling rate on output power, pressure drop and efficiency under different GMFs. The results indicate a significant enhancement in output power and pressure drop with increasing filling rate. With the rise in filling rate, the thermal uniformity zone within the heat exchanger core flow field extends towards the pipe wall, resulting in heightened temperature gradients in proximity to the pipe wall and a reduction in the thickness of the gas flow boundary layer adjacent to the pipe wall. While heat transfer performance improves, fluid disturbance intensifies, resulting in an increase in pressure drop. It's worth noting that under the positive gradient, the output power is slightly higher than in the negative gradient. However, positive gradient metal foam, as compared to the negative gradient, can reduce the pressure drop within the pipeline, with a maximum reduction of up to 3.6 % at different filling rates. By comparing Figs. 6 and 8, it can be observed that, compared to constant 40 PPI MF, the use of GMF with 10-20-40 PPI filling results in a 1.8 % reduction in output power but achieves a significant reduction of 25.6 % in pressure drop.

4.2.2. *Gradient pore porosity*

Furthermore, we examined the influence of filling gradient porosity metal foam on TEG performance. Similar to gradient PPI, we embedded metal foam with porosities of 0.9, 0.93, and 0.96 in the heat exchanger along the fluid flow direction, gradually increasing both porosity and The area of fluid flow. This configuration is referred to as the negative gradient metal foam, with the opposite defined as the positive gradient.

Fig. 9 illustrates the impact of filling rate on output power, pressure drop, and thermoelectric efficiency under gradient porosity. When compared to the 0.93 porosity, TEG's overall performance exhibits a minor decrease with both positive and negative GMF, characterized by a reduction in output power and efficiency, and an increase in pressure drop.

Similar to the trends observed with gradient PPI, negative gradient output power is lower than that of the positive gradient, with a higher pressure drop. This indicates that porosity GMF and pore density GMF exhibit similar performance characteristics. This is because increasing pore density and decreasing porosity both imply a greater presence of irregular metal frameworks within the porous copper foam. This leads to increased turbulence in the heat fluid and the gaps, which enhances heat transfer within the heat exchanger while also increasing pressure drop.

In summary, based on the results of the above study, we can conclude that arranging metal frameworks with increasing density along the fluid flow direction results in better overall performance compared to arranging metal frameworks with decreasing density.

To delve into the underlying mechanisms, we take gradient porosity as an example and calculate the average heat transfer coefficient, pressure drop, and temperature distribution for different filling regions. Fig. 10(a) and (b) display the HTCs and pressure drops in the three filling regions under different gradient porosities.

In all the configurations listed, both HTCs and pressure drops steadily decrease along the direction of fluid flow. Under negative gradient configurations, the rate of change of HTC and pressure drop in the three foam-filled regions is greater than in positive gradient configurations. For constant porosity configurations, the primary reason for changes in HTC at different locations is the temperature gradient of the heat fluid. For different GMF, since the velocity and temperature at the inlet of the heat exchanger are higher, the main pressure drop is concentrated in the first part of the heat exchanger. In the case of negative gradient configuration, the metal foam with a porosity of 0.90 is located at the inlet, whereas in positive gradient porosity, the inlet end has metal foam with a porosity of 0.96, resulting in a smaller total pressure drop. Therefore, when combining metal foams with different porosities, the total pressure drop decreases when the main pressure

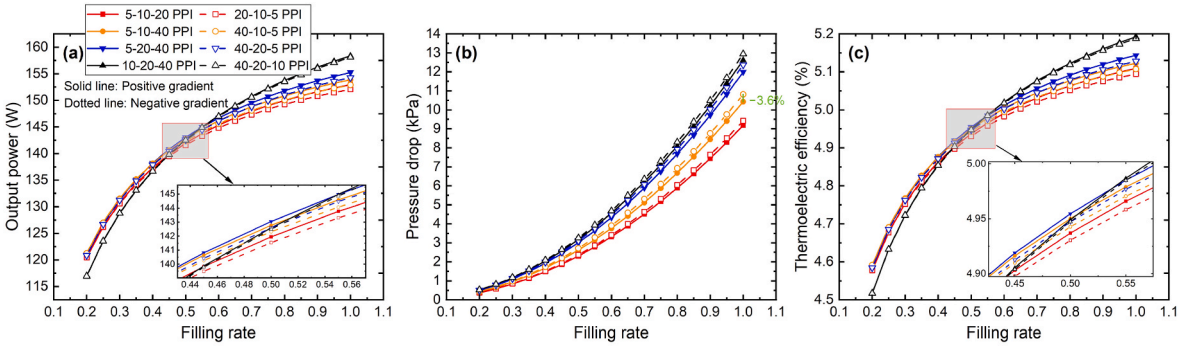

Fig. 8. Effect of filling rate on (a) output power, (b) pressure drop, and (c) thermoelectric efficiency under different PPI gradient.

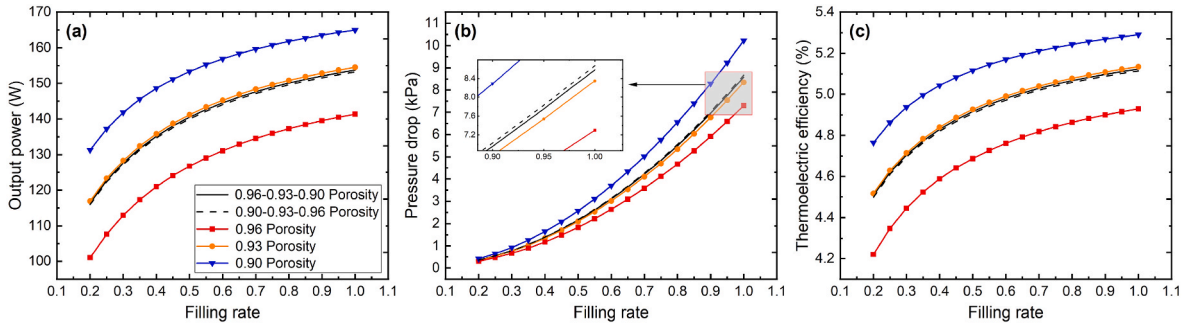

Fig. 9. Effect of filling rate on (a) output power, (b) pressure drop, and (c) thermoelectric efficiency under different porosity gradients.

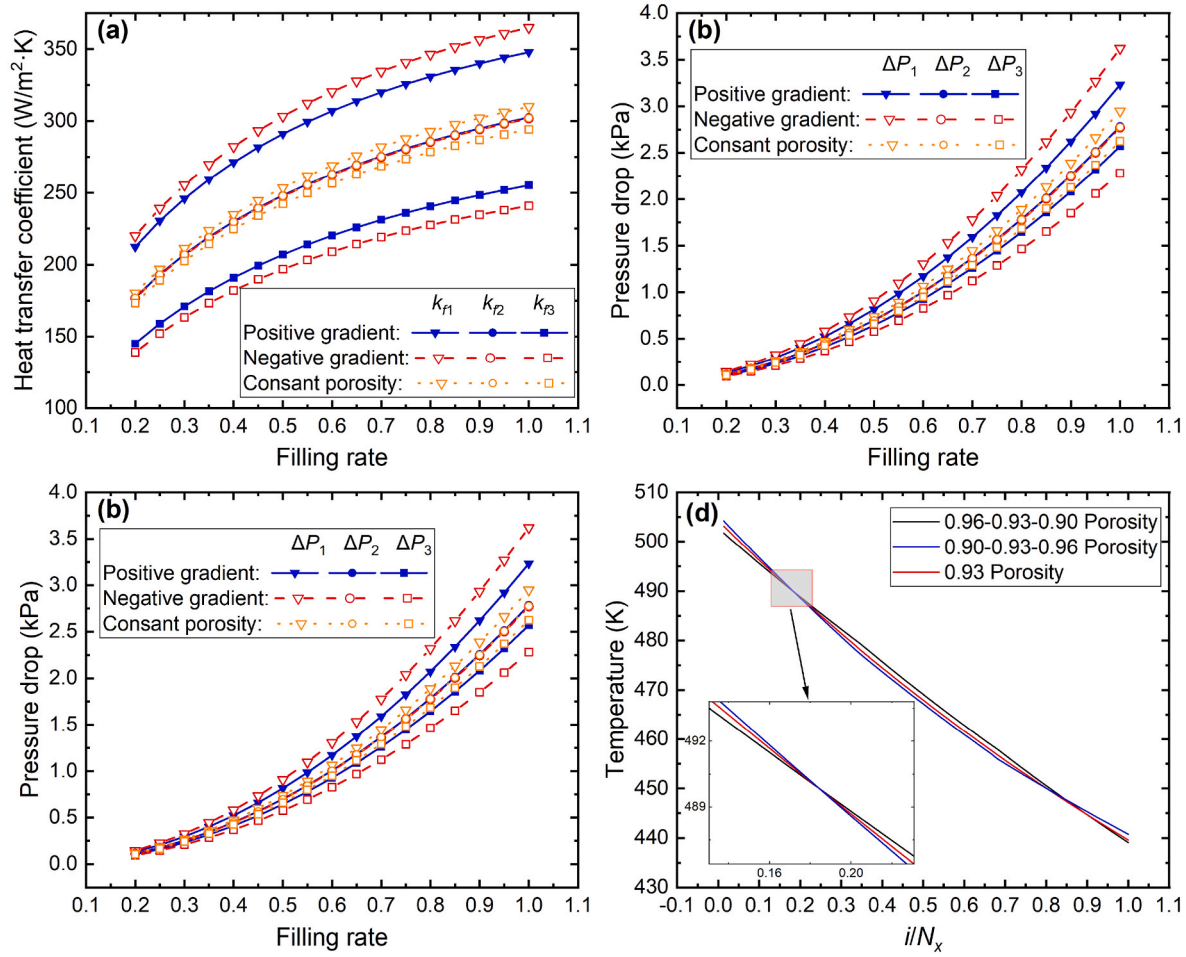

Fig. 10. Effect of filling rate on (a)HTC, (b) pressure drop, (c) voltage uniformity and (d) hot side temperature distribution under different GMF.

drop occurs in the metal foam with a larger porosity.

Fig. 10(c) demonstrates the effect of filling rate on voltage uniformity under different gradient porosity metal foam. In different GMF, voltage uniformity decreases with increasing filling rate. Positive gradient metal foam significantly enhances the voltage uniformity of the TEG, with increases of up to 23.5 % and 10.4 % compared to negative gradient porosity and constant porosity, respectively. This is in line with the conclusions reached by Bai et al. [51], who found that to achieve wall temperature uniformity in the channel, porosity should be set to linearly decrease from the inlet to the outlet. Fig. 10(d) presents the distribution of hot-side temperatures at various positions within the TEG, with normalized length indicating the location within the TEG. Here, 0 and 1 represent the exhaust inlet and outlet, respectively. For the three filling regions, the parts with smaller porosities exhibit greater temperature gradients.

4.3. Net power analysis

In the design process of automotive TEGs, it's essential to consider the TEG and the engine's output as an integrated system [52]. While it's possible to compensate for the pressure drop in the airway with an air pump, typically, the pump power is deducted from the output power, using net power as the optimization design metric [53]. The definitions for pump power, net power, and net efficiency are as follows:

$$P_p = (\Delta P m_f) / \varepsilon_f \tag{25}$$

$$P_{net} = P - P_p \tag{26}$$

$$\eta_{net} = \eta_{te} \cdot P_{net} / P \tag{27}$$

Fig. 11 depict contour plots showing the impact of filling 20 PPI metal foam and positive gradient metal foam with 5-10-20 PPI at various filling rates and air intake flows on TEG net power and net efficiency. The shaded region indicates that the power consumed by the TEG exceeds the generated power. When the net value is negative, it is not meaningful, and specific numerical values are not displayed in the graph. At low air mass flow rates, the effect of filling rate on net power is minimal. At higher mass flow rates, net power decreases with increasing filling rate, and can even become negative. This is a result of the high pressure drop caused by the metal foam. Comparing Fig. 11(a) and (c), as well as 11(b) and 11(d), reveals that positive gradient metal foam not only yields a higher maximum net power and net efficiency but also offers a range of configurations ($P_{net} > 0$) that outperform constant PPI metal foam. The maximum net power and net efficiency for positive gradient metal foam are 118.3 W and 4.3 %, respectively, which are 12.5 % and 8 % higher than those of constant 20 PPI metal foam. This demonstrates the superior performance of gradient metal foam in comparison to metal foam with a constant pore density.

5. Experimental research

To validate the superiority of GMF, experimental research was conducted using the established test platform [54]. In the heat exchanger, three regions were filled with MF having 5, 10, and 20 PPI to construct GMF. Six scenarios were evaluated, including no metal foam installation, installation of 5 PPI metal foam, installation of 10 PPI metal foam, installation of 20 PPI metal foam, positive gradient metal foam with 5-10-20 PPI, and negative gradient metal foam with 20-10-5 PPI. The effects of different filling rates (100 %, 60 %, and 30 %) were tested by filling the heat exchanger with metal foams of the same length and width as in Table 1, but with thickness of 20 mm, 12 mm, and 6 mm, respectively. Precision errors were obtained using the standard deviation of three measurements and the t-distribution, and error bars were added to the experimental data results.

Fig. 12 illustrates the impact of different GMFs on TEG output power and heat exchanger pressure drop under various filling rates. The experimental results indicate that filling metal foam can significantly enhance TEG output power, with the maximum improvement achieved by the fully filled 20 PPI metal foam configuration, resulting in an output power that is 213.5 % of the output power without metal foam filling. The lower the filling rate, the less impact pore density has on power. For the 100 % filling scenario, the output powers for these six metal foam configurations are 68.6 W, 129.6 W, 141.8 W, 146.5 W, 142.9 W, and 141.9 W, with standard deviations of 2.6 W, 3.3 W, 3.7 W, 3.8 W, 2.7 W, and 1.9 W, respectively. The output power of the positive GMF is slightly higher than that of the negative gradient, possibly because the voltage distribution in the positive gradient is more uniform, reducing parasitic power losses.

With the augmentation of pore density, the escalation in pressure drop surpasses the augmentation in TEG output power in magnitude. At

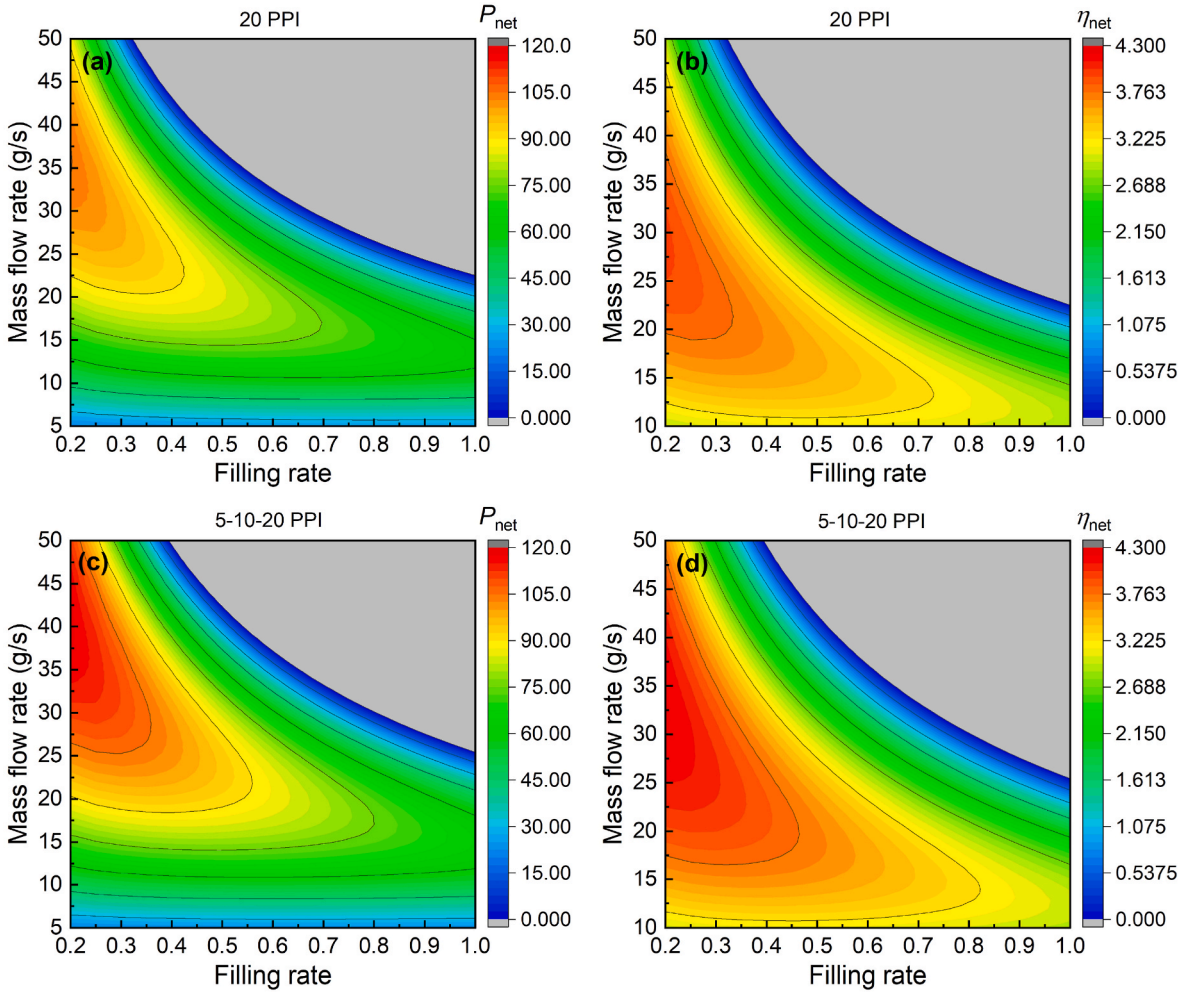

Fig. 11. Variation of net power and net efficiency with filling rate and mass flow rate for 20 PPI metal foam and 5-10-20 PPI positive gradient metal foam.

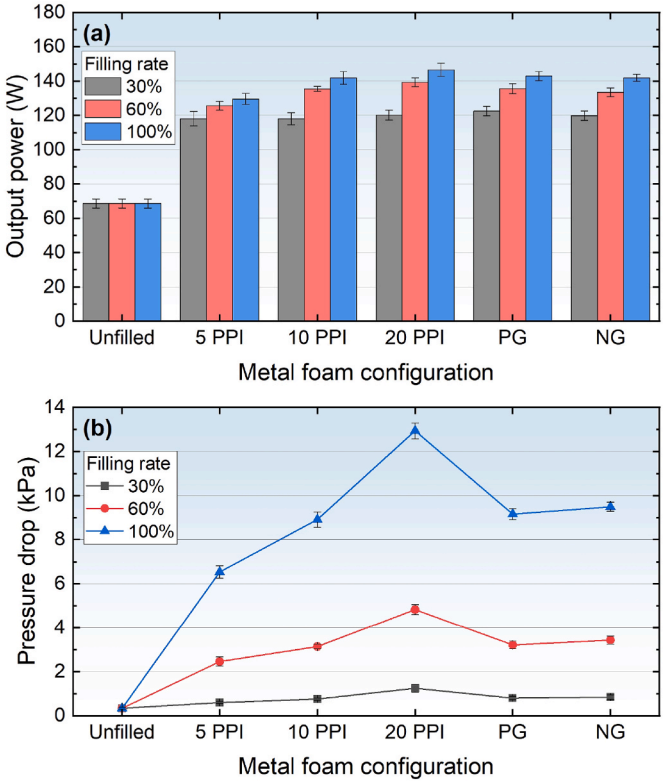

Fig. 12. Experimental results of the influence of metal foam configuration on (a) output power and (b) pressure drop at different filling rates.

different filling rates, the positive GMF configuration slightly decreases output power but significantly reduces pressure drop compared to the 20 PPI metal foam configuration. In the 100 % filling scenario, the output power of the positive gradient configuration decreased by 2.46 %, while pressure drop decreased by 29.2 %. For 30 % and 60 % filling rates, output power changes were minimal, with pressure drop reductions of 35.9 % and 33.4 %, respectively. This indicates that the GMF configuration can achieve a significant reduction in pressure drop while sacrificing only a small portion of output performance. This gradient structure is beneficial because in compact heat exchangers with high pressure drop requirements, reducing pressure drop while meeting heat transfer needs is more meaningful [55]. Furthermore, the performance of positive GMF surpasses that of negative GMF, with this effect becoming more pronounced as the metal foam filling rate increases.

In summary, the results of this experiment align with the trends in numerical simulations. They not only validate the correctness of the numerical analysis but also demonstrate that arranging metal skeletons with progressively higher density along the fluid flow direction, rather than filling the entire space with high pore density metal foam, can maintain lower exhaust pressure drop while ensuring sufficient heat transfer performance.

6. Conclusions

In this research endeavor, we have introduced a methodology for the optimization of metal foam heat exchanger configurations, aimed at enhancing the overall performance of automotive thermoelectric generators. We have crafted an analytical model for thermoelectric generators based on gradient metal foam heat exchangers, scrutinizing the impact of varying porosity and pore density of the metal foam at different filling rates on thermoelectric performance. Subsequently, we have undertaken a comprehensive investigation into the ameliorative effects of gradient metal foam on the power generation and pressure drop characteristics of thermoelectric generators, employing both numerical analysis and experimental approaches. The research findings have yielded the following conclusions.

(1) The output power and the pressure drop increase with rising pore density while decreasing with a higher porosity.
(2) Positive gradient metal foam notably enhances the voltage uniformity of the thermoelectric generator. In comparison to negative gradient and conventional metal foams, it can enhance voltage uniformity by up to 23.5 % and 10.4 %, respectively.
(3) Positive gradient metal foam with a pore density distribution of 5-10-20 PPI attains a peak net power output of 118.3 W, surpassing the net power output of constant 20 PPI metal foam by 12.5 %.
(4) Empirical evidence substantiates the superior overall performance of positive gradient metal foam. For gradient metal foams filled at 30 %, 60 %, and 100 %, power output remains relatively stable, with pressure drop reductions of 35.9 %, 33.4 %, and 29.2 %, respectively, when contrasted with constant PPI metal foam.

CRediT authorship contribution statement

Wenlong Yang: Writing – review & editing, Writing – original draft, Conceptualization. **Changjun Xie:** Writing – review & editing, Funding acquisition, Formal analysis. **Chenchen Jin:** Validation, Investigation, Data curation. **Wenchao Zhu:** Visualization, Resources, Methodology. **Yang Li:** Writing – review & editing, Validation, Resources. **Xinfeng Tang:** Supervision, Resources, Formal analysis.

Declaration of competing interest

The authors declare that they have no known competing financial interests or personal relationships that could have appeared to influence the work reported in this paper.

Acknowledgment

This work is supported by the National Natural Science Foundation of China (51977164), the Postdoctoral Fellowship Program of CPSF (GZC20232011), and the Fundamental Research Funds for the Central Universities (104972024JYS0018 and 104972024RSCbs0011).

References

[1] Y. Zou, Y. Xu, C. Zhang, A risk-averse adaptive stochastic optimization method for transactive energy management of a multi-energy microgrid, IEEE Trans. Sustain. Energy 14 (3) (2023) 1599–1611, https://doi.org/10.1109/TSTE.2023.3240184.
[2] J. Ruan, H. Cui, Y. Huang, T. Li, C. Wu, K. Zhang, A review of occluded objects detection in real complex scenarios for autonomous driving, Green Energy Intell Transp 2 (2023) 100092, https://doi.org/10.1016/j.geits.2023.100092.
[3] A.O. Ochieng, T.F. Megahed, S. Ookawara, H. Hassan, Comprehensive review in waste heat recovery in different thermal energy-consuming processes using thermoelectric generators for electrical power generation, Process Saf Environ 162 (2022) 134–154, https://doi.org/10.1016/j.psep.2022.03.070.
[4] H. Alghamdi, C. Maduabuchi, K. Okoli, A. Albaker, E. Makki, M. Alghassab, et al., Pioneering sustainable power: harnessing material innovations in double stage segmented thermoelectric generators for optimal 4E performance, Appl. Energy 352 (2023) 121885, https://doi.org/10.1016/j.apenergy.2023.121885.
[5] W. Yang, W. Zhu, B. Du, H. Wang, L. Xu, C. Xie, et al., Power generation of annular thermoelectric generator with silicone polymer thermal conductive oil applied in automotive waste heat recovery, Energy 282 (2023) 128400, https://doi.org/10.1016/j.energy.2023.128400.
[6] Z. Miao, X. Meng, L. Liu, Improving the ability of thermoelectric generators to absorb industrial waste heat through three-dimensional structure optimization, Appl. Therm. Eng. 228 (2023) 120480, https://doi.org/10.1016/j.applthermaleng.2023.120480.
[7] S. Fan, Y. Gao, A. Rezania, Thermoelectric performance and stress analysis on wearable thermoelectric generator under bending load, Renew. Energy 173 (2021) 581–595, https://doi.org/10.1016/j.renene.2021.04.009.
[8] Q. Lin, Y.-C. Chen, F. Chen, T. DeGanyar, H. Yin, Design and experiments of a thermoelectric-powered wireless sensor network platform for smart building envelope, Appl. Energy 305 (2022) 117791, https://doi.org/10.1016/j.apenergy.2021.117791.

[9] M. Ge, X. Wang, Y. Zhao, S. Wang, L. Liu, Performance analysis of vaporizer tube with thermoelectric generator applied to cold energy recovery of liquefied natural gas, Energy Convers. Manag. 200 (2019) 112112, https://doi.org/10.1016/j.enconman.2019.112112.
[10] S. Shittu, G. Li, X. Zhao, X. Ma, Review of thermoelectric geometry and structure optimization for performance enhancement, Appl. Energy 268 (2020) 115075, https://doi.org/10.1016/j.apenergy.2020.115075.
[11] M. Rakshit, D. Jana, D. Banerjee, General strategies to improve thermoelectric performance with an emphasis on tin and germanium chalcogenides as thermoelectric materials, J. Mater. Chem. A 10 (2022) 6872, https://doi.org/10.1039/d1ta10421g.
[12] X. Su, P. Wei, H. Li, W. Liu, Y. Yan, P. Li, et al., Multi-scale microstructural thermoelectric materials: transport behavior, non-equilibrium preparation, and applications, Adv. Mater. 29 (2017) 1602013, https://doi.org/10.1002/adma.201602013.
[13] S. Sakane, T. Ishibe, Y. Yukawa, Y. Nakamura, Thermoelectric properties of B-doped nanostructured bulk diamond with lowered thermal conductivity, Diam. Relat. Mater. 140 (2023) 110410, https://doi.org/10.1016/j.diamond.2023.110410.
[14] D. Luo, Y. Li, Y. Yan, X. Hu, X. Fan, W.-H. Chen, et al., Realizing ultrahigh ZT value and efficiency of the Bi2Te3 thermoelectric module by periodic heating, Energy Convers. Manag. 296 (2023) 117669, https://doi.org/10.1016/j.enconman.2023.117669.
[15] W. Yang, W. Zhu, Y. Li, C. Xie, B. Xiong, Y. Shi, et al., Global structural optimization of annular thermoelectric generators based on a dual-finite-element multiphysical model, Appl. Therm. Eng. 220 (2023) 119797, https://doi.org/10.1016/j.applthermaleng.2022.119797.
[16] W. Demeke, B. Ryu, S. Ryu, Machine learning-based optimization of segmented thermoelectric power generators using temperature-dependent performance properties, Appl. Energy 355 (2024) 122216, https://doi.org/10.1016/j.apenergy.2023.122216.
[17] W. Zhu, Z. Weng, Y. Li, L. Zhang, B. Zhao, C. Xie, et al., Theoretical analysis of shape factor on performance of annular thermoelectric generators under different thermal boundary conditions, Energy 239 (2022) 122285, https://doi.org/10.1016/j.energy.2021.122285.
[18] Q. Tan, G. Chen, Y. Sun, B. Duan, G. Li, P. Zhai, Performance of annular thermoelectric couples by simultaneously considering interface layers and boundary conditions, Appl. Therm. Eng. 174 (2020) 115301, https://doi.org/10.1016/j.applthermaleng.2020.115301.
[19] Y. Ge, K. He, L. Xiao, W. Yuan, S.-M. Huang, Geometric optimization for the thermoelectric generator with variable cross-section legs by coupling finite element method and optimization algorithm, Renew. Energy 183 (2022) 294–303, https://doi.org/10.1016/j.renene.2021.11.016.
[20] W. Yang, A. Xu, W. Zhu, Y. Li, Y. Shi, L. Huang, et al., Performance improvement and thermomechanical analysis of a novel asymmetrical annular thermoelectric generator, Appl. Therm. Eng. 237 (2024) 121804, https://doi.org/10.1016/j.applthermaleng.2023.121804.
[21] W.-H. Chen, Y.-K. Lin, D. Luo, L. Jin, A.T. Hoang, L.H. Saw, et al., Effects of material doping on the performance of thermoelectric generator with/without equal segments, Appl. Energy 350 (2023) 121709, https://doi.org/10.1016/j.apenergy.2023.121709.
[22] M.-W. Tian, I.B. Mansir, S.M. Eldin, H. Ayed, H. Loukil, N. Alkhamis, Economic and thermal performance analysis of two-stage thin-film solar thermoelectric power generator, Case Stud. Therm. Eng. 45 (2023) 103012, https://doi.org/10.1016/j.csite.2023.103012.
[23] W.-H. Chen, Y.-B. Chiou, Geometry design for maximizing output power of segmented skutterudite thermoelectric generator by evolutionary computation, Appl. Energy 274 (2020) 115296, https://doi.org/10.1016/j.apenergy.2020.115296.
[24] C. Maduabuchi, C. Eneh, A.A. Alrobaian, M. Alkhedher, Deep neural networks for quick and precise geometry optimization of segmented thermoelectric generators, Energy 263 (2023) 125889, https://doi.org/10.1016/j.energy.2022.125889.
[25] W.-H. Chen, Y.-B. Chiou, R.-Y. Chein, J.-Y. Uan, X.-D. Wang, Power generation of thermoelectric generator with plate fins for recovering low-temperature waste heat, Appl. Energy 306 (2022) 118012, https://doi.org/10.1016/j.apenergy.2021.118012.
[26] D. Luo, Z. Wu, Y. Yan, J. Cao, X. Yang, Y. Zhao, et al., Performance investigation and design optimization of a battery thermal management system with thermoelectric coolers and phase change materials, J. Clean. Prod. 434 (2024) 139834, https://doi.org/10.1016/j.jclepro.2023.139834.
[27] M.A. Zoui, S. Bentouba, D. Velauthapillai, N. Zioui, M. Bourouis, Design and characterization of a novel finned tubular thermoelectric generator for waste heat recovery, Energy 253 (2022) 124083, https://doi.org/10.1016/j.energy.2022.124083.
[28] W.-H. Chen, C.-M. Wang, L.H. Saw, A.T. Hoang, A.A. Bandala, Performance evaluation and improvement of thermoelectric generators (TEG): fin installation and compromise optimization, Energy Convers. Manag. 250 (2021) 114858, https://doi.org/10.1016/j.enconman.2021.114858.
[29] M. Ahmadian-Elmi, A. Mashayekhi, S.S. Nourazar, K. Vafai, A comprehensive study on parametric optimization of the pin-fin heat sink to improve its thermal and hydraulic characteristics, Int. J. Heat Mass Tran. 180 (2021) 121797, https://doi.org/10.1016/j.ijheatmasstransfer.2021.121797.
[30] M. He, E. Wang, Y. Zhang, W. Zhang, F. Zhang, C. Zhao, Performance analysis of a multilayer thermoelectric generator for exhaust heat recovery of a heavy-duty diesel engine, Appl. Energy 274 (2020) 115298, https://doi.org/10.1016/j.apenergy.2020.115298.
[31] J.-H. Meng, Y. Liu, X.-H. Zhu, Z.-J. Yang, K. Zhang, G. Lu, Performance enhancement for exhaust thermoelectric power generation system by using porous pin fins based on a fully automatic optimization method, Energy Convers. Manag. 273 (2022) 116404, https://doi.org/10.1016/j.enconman.2022.116404.
[32] D.R. Karana, R.R. Sahoo, Performance assessment of the automotive heat exchanger with twisted tape for thermoelectric based waste heat recovery, J. Clean. Prod. 283 (2021) 124631, https://doi.org/10.1016/j.jclepro.2020.124631.
[33] A.A. Negash, Y. Choi, T.Y. Kim, Experimental investigation of optimal location of flow straightener from the aspects of power output and pressure drop characteristics of a thermoelectric generator, Energy 219 (2021) 119565, https://doi.org/10.1016/j.energy.2020.119565.
[34] W. Zhu, A. Xu, W. Yang, B. Xiong, C. Xie, Y. Li, et al., Optimal design of annular thermoelectric generator with twisted tape for performance enhancement, Energy Convers. Manag. 270 (2022) 116258, https://doi.org/10.1016/j.enconman.2022.116258.
[35] Y. Zhao, M. Lu, Y. Li, Y. Wang, M. Ge, Numerical investigation of an exhaust thermoelectric generator with a perforated plate, Energy 263 (2023) 125776, https://doi.org/10.1016/j.energy.2022.125776.
[36] W. He, Z. Cai, R. Guo, S. Wang, L. Miao, Y. Zhao, et al., Analysis on optimal length scale of thermoelectric generators when using different circuit layouts, Appl. Therm. Eng. 231 (2023) 121006, https://doi.org/10.1016/j.applthermaleng.2023.121006.
[37] Y. Li, S. Wang, Y. Zhao, C. Lu, Experimental study on the influence of porous foam metal filled in the core flow region on the performance of thermoelectric generators, Appl. Energy 207 (2017) 634–642, https://doi.org/10.1016/j.apenergy.2017.06.089.
[38] S. Mancin, C. Zilio, A. Cavallini, L. Rossetto, Heat transfer during air flow in aluminum foams, Int. J. Heat Mass Tran. 53 (2010) 4976–4984, https://doi.org/10.1016/j.ijheatmasstransfer.2010.05.033.
[39] S. Mancin, C. Zilio, A. Diani, L. Rossetto, Air forced convection through metal foams:experimental results and modeling, Int. J. Heat Mass Tran. 62 (2013) 112–123, https://doi.org/10.1016/j.ijheatmasstransfer.2013.02.050.
[40] C. Lu, S. Wang, C. Chen, Y. Li, Effects of heat enhancement for exhaust heat exchanger on the performance of thermoelectric generator, Appl. Therm. Eng. 89 (2015) 270–279, https://doi.org/10.1016/j.applthermaleng.2015.05.086.
[41] T. Wang, W. Luan, T. Liu, S.-T. Tu, J. Yan, Performance enhancement of thermoelectric waste heat recovery system by using metal foam inserts, Energy Convers. Manag. 124 (2016) 13–19, https://doi.org/10.1016/j.enconman.2016.07.006.
[42] K. Nithyanandam, R.L. Mahajan, Evaluation of metal foam based thermoelectric generators for automobile waste heat recovery, Int. J. Heat Mass Tran. 122 (2018) 877–883, https://doi.org/10.1016/j.ijheatmasstransfer.2018.02.029.
[43] Y. Li, S. Wang, Y. Zhao, L. Yue, Effect of thermoelectric modules with different characteristics on the performance of thermoelectric generators inserted in the central flow region with porous foam copper, Appl. Energy 327 (2022) 120041, https://doi.org/10.1016/j.apenergy.2022.120041.
[44] P.H. Jadhav, G. Trilok, N. Gnanasekaran, M. Mobedi, Performance score based multi-objective optimization for thermal design of partially filled high porosity metal foam pipes under forced convection, Int. J. Heat Mass Tran. 182 (2022) 121911, https://doi.org/10.1016/j.ijheatmasstransfer.2021.121911.
[45] Z. Zhang, G. Yan, M. Sun, H. Yan, J. Zhao, Y. Song, et al., Pore-scale simulation of forced convection heat transfer in metal foams with uniform and gradient structures, Appl. Therm. Eng. 225 (2023) 120074, https://doi.org/10.1016/j.applthermaleng.2023.120074.
[46] D. Luo, Y. Yan, W.-H. Chen, X. Yang, H. Chen, B. Cao, et al., A comprehensive hybrid transient CFD-thermal resistance model for automobile thermoelectric generators, Int. J. Heat Mass Tran. 211 (2023) 124203, https://doi.org/10.1016/j.ijheatmasstransfer.2023.124203.
[47] W. He, R. Guo, S. Liu, K. Zhu, S. Wang, Temperature gradient characteristics and effect on optimal thermoelectric performance in exhaust power-generation systems, Appl. Energy 261 (2020) 114366, https://doi.org/10.1016/j.apenergy.2019.114366.
[48] K.C. Leong, L.W. Jin, Effect of oscillatory frequency on heat transfer in metal foam heat sinks of various pore densities, Int. J. Heat Mass Tran. 49 (2006) 671–681, https://doi.org/10.1016/j.ijheatmasstransfer.2005.08.015.
[49] H. Hu, Y. Zhao, Y. Li, Research progress on flow and heat transfer characteristics of fluids in metal foams, Renew. Sustain. Energy Rev. 171 (2023) 113010, https://doi.org/10.1016/j.rser.2022.113010.
[50] W. Yang, C. Jin, W. Zhu, Y. Li, R. Zhang, L. Huang, et al., Taguchi optimization and thermoelectrical analysis of a pin fin annular thermoelectric generator for automotive waste heat recovery, Renew. Energy 220 (2024) 119628, https://doi.org/10.1016/j.renene.2023.119628.
[51] X. Bai, Z. Zheng, C. Liu, A. Nakayama, Achievement of wall temperature uniformity by axially graded porous materials, Int. J. Heat Mass Tran. 197 (2022) 123335, https://doi.org/10.1016/j.ijheatmasstransfer.2022.123335.
[52] W. Zhu, W. Yang, Y. Yang, Y. Li, H. Li, Y. Shi, et al., Economic configuration optimization of onboard annual thermoelectric generators under multiple operating conditions, Renew. Energy 197 (2022) 486–499, https://doi.org/10.1016/j.renene.2022.07.124.
[53] W. Yang, W. Zhu, Y. Li, L. Zhang, B. Zhao, C. Xie, et al., Annular thermoelectric generator performance optimization analysis based on concentric annular heat

exchanger, Energy 239 (2022) 122127, https://doi.org/10.1016/j.energy.2021.122127.
[54] W. Yang, C. Jin, W. Zhu, C. Xie, L. Huang, Y. Li, et al., Innovative design for thermoelectric power generation: two-stage thermoelectric generator with variable twist ratio twisted tapes optimizing maximum output, Appl. Energy 363 (2024) 123047, https://doi.org/10.1016/j.apenergy.2024.123047.
[55] D. Luo, Y. Yan, Y. Li, X. Yang, H. Chen, Exhaust channel optimization of the automobile thermoelectric generator to produce the highest net power, Energy 281 (2023) 128319, https://doi.org/10.1016/j.energy.2023.128319.